OPEN ACCESS
Journal of Innovative Optical Health Sciences
Vol. 16, No. 5 (2023) 2350002 (14 pages)

DOI: 10.1142/S1793545823500025

World Scientific
www.worldscientific.com

Comparison of uniform resampling and nonuniform sampling direct-reconstruction methods in *k*-space for FD-OCT

Yanrong Yang[*,§,¶], Yun Dai[*,§,¶], Yuehua Zhou[*,¶] and Yaliang Yang[†,‡,‖]

[*]*College of Ophthalmology*
Chengdu University of Traditional Chinese Medicine
Chengdu 610075, P. R. China

[†]*Institute of Optics and Electronics, Chinese Academy of Sciences*
Chengdu 610209, P. R. China

[‡]*Key Laboratory of Adaptive Optics, Chinese Academy of Sciences*
Chengdu 610209, P. R. China

[§]*Key Laboratory of Sichuan Province Ophthalmopathy Prevention & Cure and Visual Function Protection with TCM*
Chengdu 610075, P. R. China

[¶]*Ineye Hospital of Chengdu University of TCM*
Chengdu 610075, P. R. China
[‖]*ylyang@ioe.ac.cn*

Received 25 October 2022
Revised 13 December 2022
Accepted 13 December 2022
Published 11 March 2023

The nonuniform distribution of interference spectrum in wavenumber *k*-space is a key issue to limit the imaging quality of Fourier-domain optical coherence tomography (FD-OCT). At present, the reconstruction quality at different depths among a variety of processing methods in *k*-space is still uncertain. Using simulated and experimental interference spectra at different depths, the effects of common six processing methods including uniform resampling (linear interpolation (LI), cubic spline interpolation (CSI), time-domain interpolation (TDI), and K-B window convolution) and nonuniform sampling direct-reconstruction (Lomb periodogram (LP) and nonuniform discrete Fourier transform (NDFT)) on the reconstruction quality of FD-OCT were quantitatively analyzed and compared in this work. The results obtained by using simulated and experimental data were coincident. From the experimental results, the averaged peak intensity, axial resolution, and signal-to-noise ratio (SNR) of NDFT at depth from 0.5 to 3.0 mm were improved by about 1.9 dB, 1.4 times, and 11.8 dB, respectively, compared to the averaged indices of all the uniform resampling methods at all depths. Similarly, the improvements of the

[‖]Corresponding author.

above three indices of LP were 2.0 dB, 1.4 times, and 11.7 dB, respectively. The analysis method and the results obtained in this work are helpful to select an appropriate processing method in k-space, so as to improve the imaging quality of FD-OCT.

Keywords: Optical coherence tomography; signal processing; uniform resampling; nonuniform sampling direct-reconstruction; reconstruction quality.

1. Introduction

Optical coherence tomography (OCT)[1] can obtain high-resolution cross-sectional images of probed samples in noninvasive and noncontact ways, and has been widely used for *in vivo* high-resolution imaging of eye, skin, cardiovascular plaque, gastrointestinal tract, etc.[2–5] At present, the mainstream OCT technology is Fourier-domain optical coherence tomography (FD-OCT),[6] which has the advantages of high speed, high signal-to-noise ratio (SNR), and high system stability. FD-OCT can be divided into spectral-domain (SD-) and swept source (SS-) OCT according to the different acquisition methods of interference spectrum.[7] The former uses a continuous broadband light source and spectroscopic technology mainly composed of a spectral dispersive element and a linear array detector. The latter adopts the time-division spectrum technology of sweep source and a point detector. They have the same principle and similar data processing flow and methods, and thus are no longer distinguished in this paper and referred to as FD-OCT.

FD-OCT obtains the object signal based on the Wiener–Khintchine theorem: Wavenumber $\boldsymbol{k}$ and axial depth $\boldsymbol{z}$ are a Fourier transform (FT) pair. Therefore, the reflectivity profile along depth $\boldsymbol{z}$ within the sample can be reconstructed from interference spectrum $\boldsymbol{I}(\boldsymbol{k})$ through inverse discrete FT (IDFT). However, the collected interference spectrum is the function of wavelengths $\boldsymbol{\lambda}$, which needs to be converted into k-space before performing IDFT. Even the output $\boldsymbol{\lambda}$ of a light source is a linear distribution, nonuniform distribution in k-space is obtained according to the relationship $k = 2\pi/\lambda$.[8] Direct IDFT on $\boldsymbol{I}(\boldsymbol{k})$ will cause the reconstruction quality to degrade rapidly with increased imaging depth.[9] The key to avoid this problem lies in how to perform uniform resampling[10,11] or nonuniform sampling direct-reconstruction[12–14] in k-space.

k-space uniform resampling can be realized by hardware,[15–19] but it is difficult to find an acquisition card to meet the frequency range of k-clock signal, and is unable to flexibly adjust parameters to meet different application requirements. In addition, a small part of the output light signal of source can be delivered to a reference interferometer such as a Mach–Zehnder interferometer,[20] and a uniform calibration signal in k-space can be extracted by using methods such as phase detection,[21] zero-crossing detection[22] or polynomial fitting.[23] However, the main defect is that it needs to accurately match the time delay between the reference clock and the interference spectrum.

In addition to the hardware method, digital signal processing has become a common calibration method in k-space, including uniform resampling and nonuniform sampling direct-reconstruction methods, which has the advantages of low cost and flexibility. Uniform resampling method mainly includes linear interpolation (LI),[24] cubic spline interpolation (CSI),[25] time-domain interpolation (TDI),[26] and Kaiser–Bessel window convolution (KBWC).[27] Direct-reconstruction method mainly includes Lomb periodogram (LP)[28] and nonuniform discrete Fourier transform (NDFT).[29] Interpolation method is an effective way to improve the reconstruction quality.[30] Liu *et al.*[31] demonstrated that CSI had the highest cost performance. Eigenwillig *et al.*[16] presented that the SD zero-filling method is more time-consuming compared to the interpolation method. Vergnole *et al.*[32] built a SS-OCT platform to experimentally compare and analyze the reconstruction performance of LI, CSI, KBWC, LP, and NDFT. It was concluded that KBWC with an optimized window size has the best performance in time-consuming and imaging quality. It remains to be verified whether above the results are universal, at least they need to be considered on the influence of noise. Therefore, if simulated and experimental data can be used to evaluate the reconstruction performance of above the methods, the obtained results will be more accurate and universal.

Based on the above background, the basic principle of uniform resampling (LI, CSI, TDI, KBWC) and nonuniform sampling direct-reconstruction (LP,

NDFT) methods is presented in this work. Using interference spectra at different depths obtained by numerical simulation and practical experiment, the influences of these methods on the reconstruction performance are quantitatively evaluated by using the peak intensity, SNR, and axial resolution δ of point spread function (PSF). The obtained results are helpful to select an appropriate k-space data processing method, so as to improve the reconstruction quality of FD-OCT in practical applications.

2. Materials and Methods

2.1. *Effect of k-space uniform resampling on reconstruction quality*

In FD-OCT, multidimensional image is reconstructed by formatting multiple one-dimensional depth profiles (i.e., A-scan signals) corresponding to different lateral positions through a scanning device. Therefore, A-scan signal is the basic unit of FD-OCT. Simulated $\boldsymbol{I}(\boldsymbol{k})$ at different depths can be obtained by changing the optical path difference between reference and sample arms, and the $\boldsymbol{I}(\boldsymbol{k})$ at an optical path difference of 1 mm as an example is shown in Fig. 1(a) (reshaped with Hamming window, the same below). Performing IDFT on the $\boldsymbol{I}(\boldsymbol{k})$ in k-space to reconstruct A-scan signals would generate point spread functions (PSFs) at different depths, which are shown in Fig. 1(b).

In the simulation, $\boldsymbol{\lambda}$ is uniformly sampled within $\lambda_{\min} \sim \lambda_{\max}$, i.e.,

$$\boldsymbol{\lambda} = \lambda_{\min} + \frac{n}{N-1}(\lambda_{\max} - \lambda_{\min}), \tag{1}$$

where n is the sampling point and $N = 1024$ is the length. According to $\boldsymbol{k} = \boldsymbol{2\pi/\lambda}$, $\boldsymbol{k}$ is nonuniform in k-space,

$$\boldsymbol{k} = \frac{2\pi}{\lambda} = \frac{2\pi}{\lambda_{\min} + n(\lambda_{\max} - \lambda_{\min})/(N-1)}. \tag{2}$$

Thus, $\boldsymbol{I}(\boldsymbol{k})$ in k-space can be expressed as follows[33]:

$$\boldsymbol{I}(\boldsymbol{k}) = 2P \times \sum_n \sqrt{R_r}\sqrt{\boldsymbol{R_s}(z_n)}\cos(2kz_n), \tag{3}$$

where $2z_n$ is the optical path difference, R_r is the reflectance of the reference arm, and $\boldsymbol{R_s}(z_n)$ is the reflectance at depth z_n within the sample. The signal amplitudes of the reference and sample arms are the same of P. $\boldsymbol{I}(\boldsymbol{k})$ is shown in Fig. 1(a) with the black line.

According to the Wiener–Khintchine theorem, $\boldsymbol{I}(\boldsymbol{k})$ and $\boldsymbol{R_s}(\boldsymbol{z})$ are FT relations, but the premise for calculating IDFT is that $\boldsymbol{I}(\boldsymbol{k})$ is uniformly sampled. As shown in Fig. 1(b), the black lines are the PSFs obtained by performing IDFT on $\boldsymbol{I}(\boldsymbol{k})$ under nonuniform sampling in k-space. It can be seen that the axial resolution of the reconstruction is decreased rapidly with increasing depth.

In order to improve the reconstruction quality, $\boldsymbol{I}(\boldsymbol{k})$ should be resampled or preprocessed in k-space. Uniform resampling in k-space will obtain $\boldsymbol{k}_{\text{even}}$,

$$\begin{aligned}\boldsymbol{k}_{\text{even}} &= k_{\max} - \frac{m}{M-1}(k_{\max} - k_{\min}) \\ &= \frac{2\pi}{\lambda_{\min}} - \frac{m}{M-1}\left(\frac{2\pi}{\lambda_{\min}} - \frac{2\pi}{\lambda_{\max}}\right),\end{aligned} \tag{4}$$

where M (its value corresponds to oversampling factor) is the resampling length and m is the resampling point. The interpolation position $\boldsymbol{n}_{\text{even}}$

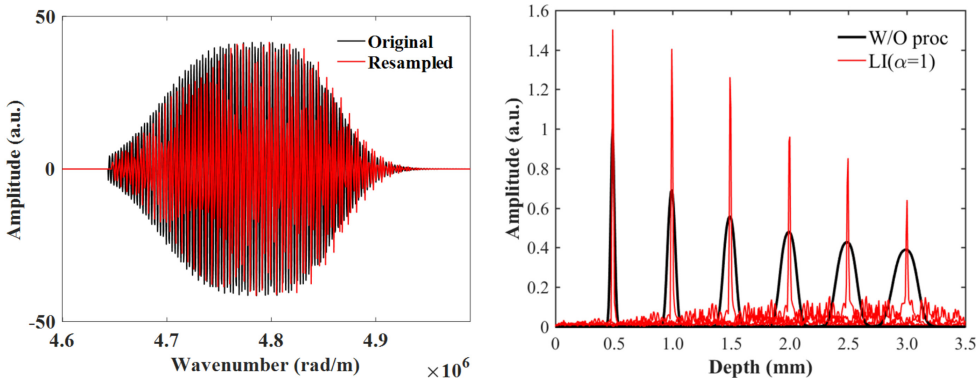

(a) (b)

Fig. 1. (a) Simulated interference spectrum $\boldsymbol{I}(\boldsymbol{k})$ in k-space, (b) PSFs at different depths reconstructed without processing (W/O proc) and with LI in k-space. All PSFs in this work are normalized relative to the peak intensity at depth of 0.5 mm under W/O proc.

can be obtained by

$$\boldsymbol{n}_{\text{even}} = \left\{\left[\frac{1}{\lambda_{\min}} - \frac{m}{M-1}\left(\frac{1}{\lambda_{\min}} - \frac{1}{\lambda_{\max}}\right)\right]^{-1} - \lambda_{\min}\right\} \times \frac{N-1}{\lambda_{\max} - \lambda_{\min}}. \quad (5)$$

The uniformly resampled spectrum $\boldsymbol{I}(\boldsymbol{k}_{\text{even}})$ can be obtained by LI method, and then the reconstructed PSFs are shown in Fig. 1(b) (in the red lines). The result shows that the axial resolution after uniform resampling almost remains the same within the depth range of 3 mm. Thus, the data processing in k-space can greatly improve the reconstruction quality of FD-OCT.

2.2. *Uniform resampling methods in k-space*

The k-space in nonuniform sampling can be transformed to $\boldsymbol{k}_{\text{even}}$ by uniform resampling, and the length will change from N to M, so the oversampling factor is defined as $\alpha = M/N$.

Using the sampling data nearest to $\boldsymbol{k}_{\text{even}}$, the resampled signal can be obtained by LI,

$$\boldsymbol{I}(\boldsymbol{k}_{\text{even}}) = I(k_n) + \frac{k_{\text{even}} - k_n}{k_{n+1} - k_n}(I(k_{n+1}) - I(k_n)), \quad (6)$$

where k_n is the nonuniform sampling point in k-space.

Using the sampling data adjacent to $\boldsymbol{k}_{\text{even}}$ and its second derivative, the resampled signal can be obtained by CSI,[34]

$$\boldsymbol{I}(\boldsymbol{k}_{\text{even}}) = a \times I(k_n) + b \times I(k_{n+1}) + c \times I''(k_n) + d \times I''(k_{n+1}), \quad (7)$$

where $I''(k_n)$ and $I''(k_{n+1})$ are the second derivatives of $I(k_n)$ and $I(k_{n+1})$, respectively. $a = 1 - b$, b, c, and d are calculated by

$$b = \frac{k_{\text{even}} - k_n}{k_{n+1} - k_n}, \quad (8)$$

$$c = \frac{1}{6}(a^3 - a)(k_n - k_{n+1})^2, \quad (9)$$

$$d = \frac{1}{6}(b^3 - b)(k_n - k_{n+1})^2. \quad (10)$$

TDI is an improvement of the zero-filling interpolation method in time-domain, which requires zero-filling interpolation in time-domain and uniform resampling in frequency-domain. It reduces the computational efficiency. Considering the conjugate symmetry of real FT, the uniformly resampled $I(k_{\text{even}})$ with TDI can be expressed as follows[35]:

$$\boldsymbol{I}(\boldsymbol{k}_{\text{even}}) = \frac{1}{\alpha \times M + 1} \times \sum_{n=0}^{N} I(k)\left\{1 + 2\sum_{i=1}^{M/2}\cos\frac{2\pi}{M} i\left(\frac{n_{\text{even}}}{\alpha} - n\right)\right\}. \quad (11)$$

In fact, Eq. (11) only needs several values at $n = n_{\text{even}}/\alpha$ to determine the cosine weight, for example the value of n is taken in the range of window size $W = 11$ in our experiment.

KBWC obtains the resampled data by using a K-B window function as convolution kernel. The coefficient of K-B window[36] is $C(k_{\text{even}}, k_n)$,[37]

$$C(k_{\text{even}}, k_n) = B_0\left(\beta\sqrt{1 - \left(2\frac{k_{\text{even}} - k_n}{\delta k \times L}\right)^2}\right)\Big/ L, \quad (12)$$

where $\beta = \pi\sqrt{\left(\frac{L^2}{\alpha^2}\right)(\alpha - 0.5)^2 - 0.8}$, $\delta k = \frac{k_{\max} - k_{\min}}{N \times \alpha}$, and $B_0(\bullet)$ is the first kind of zero-order modified Bessel function. The typical value of length L is 3–8. Then the uniform resampling signal is as follows:

$$\boldsymbol{I}(\boldsymbol{k}_{\text{even}}) = \sum_{n=1}^{L} I(k_n) C(k_{\text{even}}, k_n). \quad (13)$$

As a summary, the resampled interference spectrum $\boldsymbol{I}(\boldsymbol{k}_{\text{even}})$ is first obtained by using LI, CSI, TDI, and KBWC methods, and then the A-scan signal $\boldsymbol{R}(\boldsymbol{z})$ is reconstructed by performing IDFT on the $I(k_{\text{even}})$,

$$\boldsymbol{R}(\boldsymbol{z}) = \text{IDFT}[\boldsymbol{I}(\boldsymbol{k}_{\text{even}})]. \quad (14)$$

2.3. *Nonuniform sampling direct–reconstruction methods in k-space*

LP developed for estimating the power spectrum of time-series signal is a DFT under nonuniform sampling.[28] Based on the principle of DFT, the data for each frequency can be calculated with an integration in time-domain. Thus, LP uses a least-square fitting of a sinusoid to perform FFT. The fitted data

will have a well-defined statistical behavior. The information $\boldsymbol{R}(\boldsymbol{z})$ can be directly reconstructed from the nonuniform sampling signal $\boldsymbol{I}(\boldsymbol{k})$.[34]

$$|\boldsymbol{R}(\boldsymbol{z})|^2 = \frac{2}{N}\left\{\begin{array}{l}\dfrac{\left|\sum_n^N I(k_n)\cos 2z(k_n-\bar{k})\right|^2}{\sum_n^N \cos^2 2z(k_n-\bar{k})} \\ +\dfrac{\left|\sum_n^N I(k_n)\sin 2z(k_n-\bar{k})\right|^2}{\sum_n^N \sin^2 2z(k_n-\bar{k})}\end{array}\right\}, \tag{15}$$

$$\tan 4z\bar{k} = \frac{\sum_n^N \sin 4zk_n}{\sum_n^N \cos 4zk_n}, \tag{16}$$

where $\bar{k}$ can be pre-calculated by Eq. (16).

NDFT is another direct-reconstruction method[38] which has been theoretically explained and can be used as a benchmark for the nonuniform sampling. Its expression is as follows:

$$\begin{aligned}\boldsymbol{R}(\boldsymbol{z}) &= \frac{2}{N}\sum_n^N I(k_n)\gamma_n^q, \gamma_n \\ &= \exp\left(j\frac{2\pi}{k_{\max}-k_{\min}}k_n\right),\end{aligned} \tag{17}$$

where q is from 0 to $N-1$. The expression in matrix form is $\boldsymbol{R} = \boldsymbol{E}\times\boldsymbol{I}$,

$$\boldsymbol{I} = \begin{pmatrix} I(k_0) \\ I(k_1) \\ \cdots \\ I(k_{N-1}) \end{pmatrix}, \quad \boldsymbol{E} = \begin{pmatrix} \gamma_0^0 & \gamma_1^0 & \cdots & \gamma_{N-1}^0 \\ \gamma_0^1 & \gamma_1^1 & \cdots & \gamma_{N-1}^1 \\ \cdots & \cdots & \cdots & \cdots \\ \gamma_0^{N-1} & \gamma_1^{N-1} & \cdots & \gamma_{N-1}^{N-1} \end{pmatrix},$$
$$\boldsymbol{R} = \begin{pmatrix} R(z_0) \\ R(z_1) \\ \cdots \\ R(z_{N-1}) \end{pmatrix}, \tag{18}$$

where $\boldsymbol{E}$ is the Vandermond matrix.

2.4. *Evaluation indices of reconstruction performance*

In this work, the peak intensity, axial resolution δ, and SNR of PSFs at different depths are taken as the evaluation indices to quantitatively analyze and compare the effects of the methods on the reconstruction quality of FD-OCT. SNR is defined as follows:

$$\mathrm{SNR} = 20\log\left(\frac{A_S}{A_N}\right), \tag{19}$$

where A_S is the mean value within the full width at half maximum (FWHM) of PSF. Different from Ref. 32, the noise A_N is defined as the mean value outside the twice range of FWHM. δ is expressed by FWHM of PSF.

2.5. *Comparison of computational complexity*

In order to evaluate the real-time performance of the methods for an A-scan signal, computational complexities of the calibration in k-space and IDFT when $\alpha = 1$ (M and $N = 1024$, $W = 11$, $L = 5$) are shown in Table 1. Compared to the complexity of W/O proc, the low computational costs of the uniform resampling are mainly contributed to the fast Fourier transformation and the window size of the weighting factors. The significant higher costs of NDFT and LP are related to the matrix operation. However, using a fast algorithm such as Lagrange interpolating polynomials[34] or using GPUs CUDA library can get further computational optimization in NDFT and LP.

3. Results and Discussion

3.1. *Simulated interference spectra without and with noise*

The FD-OCT system simulated with the parameters shown in Table 2 is consistent with the

Table 1. Computational complexity analysis.

	Calibration in k-space			IDFT		
Method	Real addition	Real multiplication	Cosine	Real addition	Real multiplication	Complexity ratio
W/O proc	0	0	0	$N\log_2 N$	$0.5\,N\log_2 N$	1
LI	$2M$	M	0	$N\log_2 N$	$0.5\,N\log_2 N$	1.20
CSI	$8M$	$9M$	0	$N\log_2 N$	$0.5\,N\log_2 N$	2.13
TDI	$NW + M(W-1)$	$(N/2+2M)W + M$	NW/2	$N\log_2 N$	$0.5\,N\log_2 N$	4.67
KBWC	$(L-1)M$	LM	0	$N\log_2 N$	$0.5\,N\log_2 N$	1.60
NDFT	$N(2N-1)$	$2N\times N$	0	0	0	273.00
LP	$(2N-1)N$	$(2N+4)N$	0	0	0	273.27

Table 2. Parameters of FD-OCT system used for simulation.

Parameter	Value
Sweeping rate	50 kHz
Duty ratio	0.45
Center wavelength	1312 nm
Wavelength range	1259–1366
3 dB range	70 nm

SS-OCT experimental system. By axial moving the reflective surface position of the sample, the interference spectra without noise at depth z of 0.5, 1.0, 1.5, 2.0, 2.5, and 3.0 mm were generated and shown in Figs. 2(a)–2(f).

To quantify the influence of noise, the SNR of the interference spectrum is defined as follows:

$$\mathrm{SNR}_{\mathrm{IS}} = 10\lg\left(N\frac{\sum_k \boldsymbol{I}^2_{\mathrm{sample}}(k)}{\sum_k \boldsymbol{I}^2_{\mathrm{noise}}(k)}\right), \tag{20}$$

where $I_{\mathrm{sample}}(k)$ and $I_{\mathrm{noise}}(k)$ are the amplitudes of the interference spectrum and the noise, respectively. Noise agrees with the random normal distribution and the sources include light intensity fluctuation, spectral sweep error, sampling error, detector noise, optical path matching error, phase random error, central wavelength or central wavenumber fluctuation,[39] etc. When $\mathrm{SNR}_{\mathrm{IS}} = -10$ dB

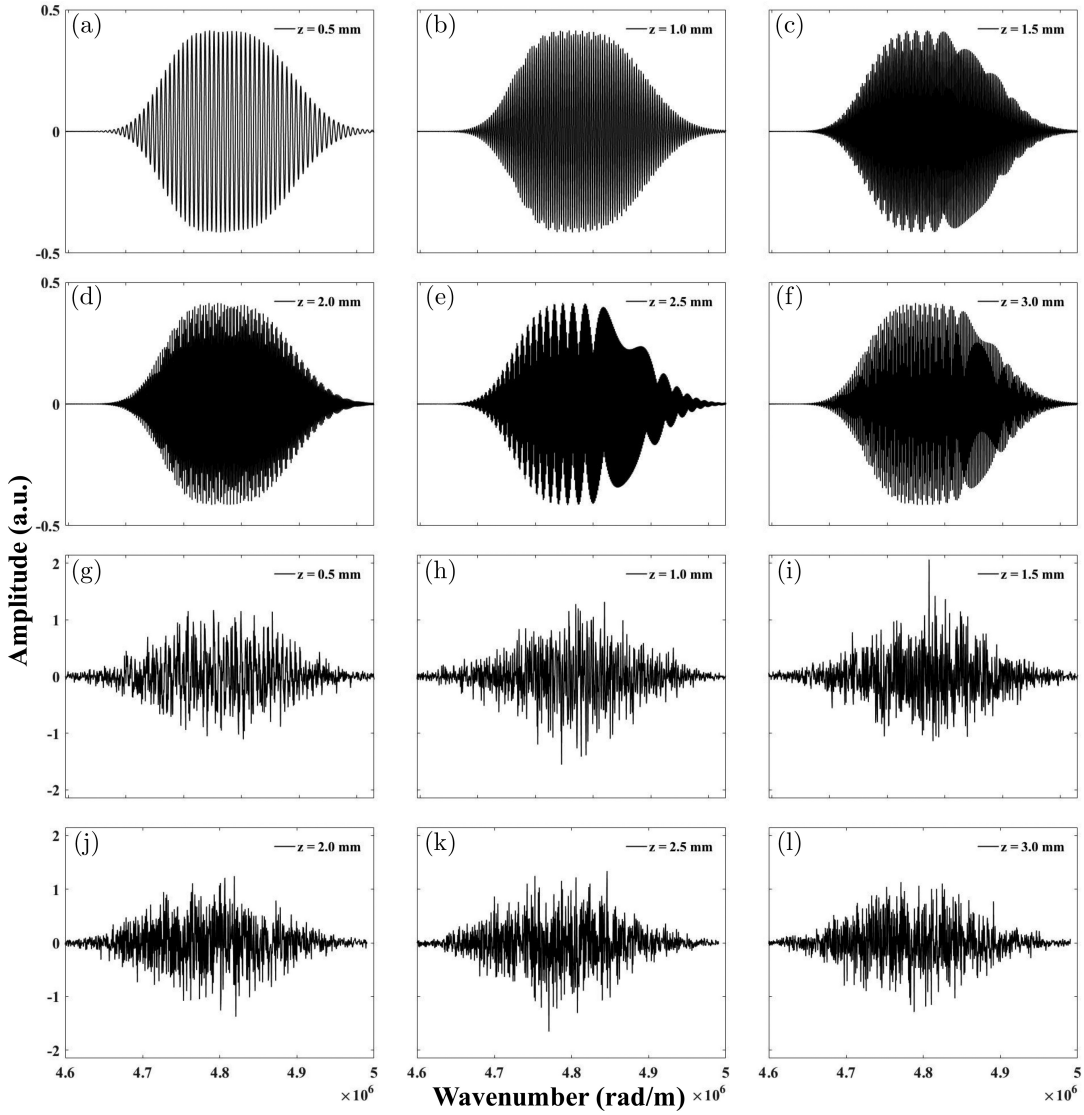

Fig. 2. $I(k)$ at different depths under without (a)–(f) and with (g)– (l) noise in SNR_{IS} of -10 dB.

(the noise intensity is close to the signal's), the $\boldsymbol{I}(\boldsymbol{k})$ at different depths are shown in Figs. 2(g)–2(l).

3.2. *PSFs without and with processing method in k-space*

The reconstructed PSFs at different depths can be obtained from the $\boldsymbol{I}(\boldsymbol{k})$ shown in Fig. 2 after IDFT in k-space. Without processing (W/O proc), the PSFs without and with noise in $\mathrm{SNR_{IS}}$ of -10 dB are shown in Figs. 3(a) and 3(b), respectively. It can be seen that the peak intensity decreases with the imaging depth (down about 4.2 dB within 3 mm) under without noise. And δ also decreases rapidly with the imaging depth. When $\mathrm{SNR_{IS}} = -10$ dB, the background noise of the PSF increases obviously, and the object signal cannot be reconstructed effectively when the imaging depth is greater than 1.5 mm.

Therefore, k-space data processing method is the key to improve the reconstruction quality. For this reason, uniform resampling and nonuniform sampling direct-reconstruction methods in k-space are used to extract the depth profile of sample. The results are shown in Fig. 4.

Without noise, the reconstructed results after uniform resampling and nonuniform sampling direct-reconstruction are shown in Figs. 4(a)–4(f), respectively. Figures 4(g)–4(l) show the PSFs at $\mathrm{SNR_{IS}} = -10$ dB. Figures 4(g)–4(j) show the reconstructed results after uniform resampling, and Figs. 4(k) and 4(l) show the reconstructed results of NDFT and LP, respectively. It can be seen that the PSF broadening with the imaging depth can be significantly eliminated after the k-space data processing, so as to improve the reconstruction quality.

From Figs. 4(a)–4(f), it is found that the reconstruction quality of LP and NDFT is significantly better than that of the other methods. In addition, the reconstructed results of TDI and KBWC ($\alpha = 2$) are better than those of the other uniform resampling methods. Compared to LP and NDFT, the uniform resampling is easy to introduce interpolation noise, shown as the PSFs in Figs. 4(a)–4(d). With the noise in $\mathrm{SNR_{IS}}$ of -10 dB (Figs. 4(g)–4(l)), NDFT, LP, TDI ($\alpha = 1$, $\alpha = 2$) and KWBC ($\alpha = 2$) can accurately reconstruct the structures within 3 mm (SNR > 13 dB).

3.3. *Comparison of results using simulated data*

Figures 5(a)–5(c) show the peak intensity, δ and SNR of the PSFs without noise. It can be seen that all the data processing methods can improve the peak intensity and δ. The peak intensities of LP, NDFT, TDI ($\alpha = 1$, $\alpha = 2$), and KWBC ($\alpha = 1$) keep above 0 dB and their fall-off within 3 mm is less than 6 dB. δ of all the methods are relatively stable within 3 mm. In addition, LI ($\alpha = 1$, $\alpha = 2$), CSI ($\alpha = 1$, $\alpha = 2$) and KWBC ($\alpha = 1$) cause obvious noise. The SNRs of LP, NDFT, TDI ($\alpha = 1$, $\alpha = 2$) and KWBC ($\alpha = 1$, $\alpha = 2$) keep above 25 dB within 3 mm. The detailed δ values for the data without noise are listed in Table 3. It can be seen that the improvements of the averaged peak intensity, δ and SNR of NDFT at depths from 0.5 to 3.0 mm are 2.4 dB, 1.3 times and 14.3 dB, respectively,

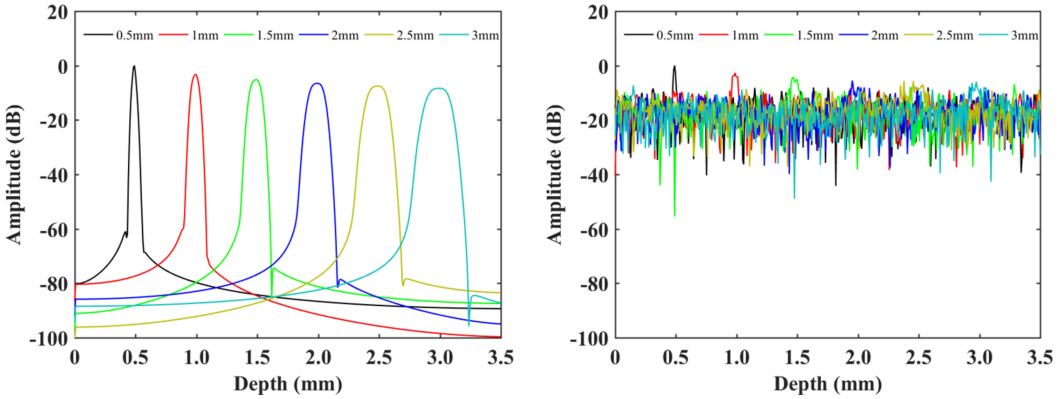

(a) (b)

Fig. 3. Reconstructed PSFs without data processing in k-space under (a) without and (b) with noise.

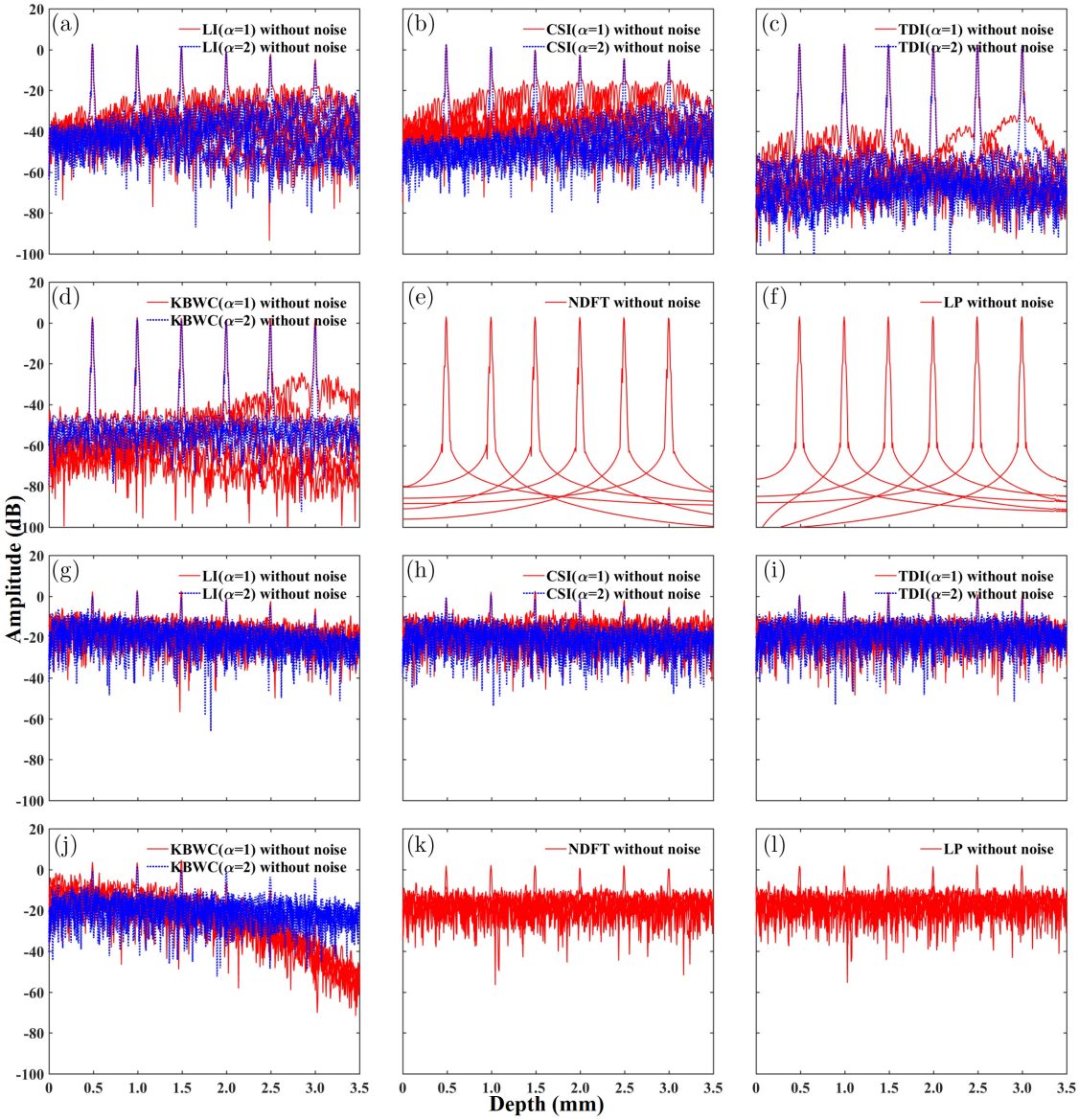

Fig. 4. PSFs of simulated mirror sample at different depths obtained with different methods under (a)–(f) without and (g)–(l) with noise.

compared to the averaged indices of all the uniform resampling methods at all depths. Similarly, the improvements of the above three indices of LP are 2.7 dB, 0.7 times, and 33.5 dB, respectively.

Figures 5(d)–5(f) show the peak intensity, δ and SNR of PSFs at $\mathrm{SNR}_{IS} = -10$ dB. It can be seen that all the methods except KWBC ($\alpha = 1$) can accurately reconstruct the structures within 3 mm. Relative to W/O proc, the reconstructed results of LP, NDFT, and TDI ($\alpha = 1$, $\alpha = 2$) have improved peak intensity within 3 mm. The peak intensities of LP, NDFT, and TDI ($\alpha = 1$) can be kept above 0 dB and their fall-off within 3 mm are less than 6 dB. The SNRs of all methods except LI ($\alpha = 1$), CSI ($\alpha = 1$), and KWBC ($\alpha = 1$) are also improved within 3 mm. The changes of SNRs are less than 6 dB for LP, NDFT, TDI ($\alpha = 1$, $\alpha = 2$), KWBC ($\alpha = 2$) and CSI ($\alpha = 2$). In addition, the δ of NDFT, KWBC ($\alpha = 2$), CSI ($\alpha = 2$), LP and TDI ($\alpha = 1$) are stable within 3 mm. The detailed δ values for the data with noise in $\mathrm{SNR}_{\mathrm{IS}}$ of -10 dB are shown in Table 3. In this case, the improvements of the averaged peak intensity, δ and SNR of NDFT at depths from 0.5 to 3.0 mm are 2.9 dB, 1.4 times and 2.2 dB, respectively, compared to the averaged indices of all the uniform resampling

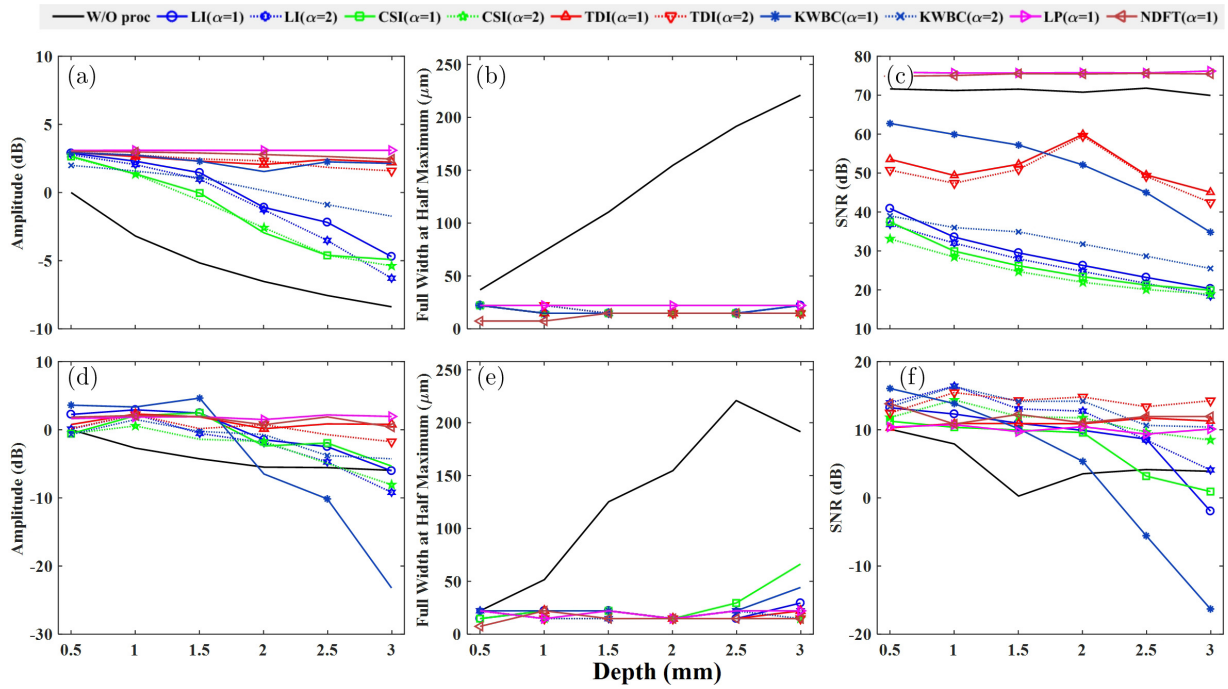

Fig. 5. Peak intensity, δ, and SNR of PSFs at different depths using simulated data under (a)–(c) without and (d)–(f) with noise.

Table 3. Detailed δ values of different methods using simulated data (units: μm).

	Depth (mm)	W/O proc	LI ($\alpha=1$)	LI ($\alpha=2$)	CSI ($\alpha=1$)	CSI ($\alpha=2$)	TDI ($\alpha=1$)	TDI ($\alpha=2$)	KWBC ($\alpha=1$)	KWBC ($\alpha=2$)	NDFT	LP
Without noise	0.5	36.8	22.1	22.1	22.1	22.1	22.1	22.1	22.1	22.1	7.4	22.1
	1.0	73.7	14.7	14.7	14.7	14.7	14.7	22.1	14.7	22.1	7.4	22.1
	1.5	110.5	14.7	14.7	14.7	14.7	14.7	14.7	14.7	14.7	14.7	22.1
	2.0	154.7	14.7	14.7	14.7	14.7	14.7	14.7	14.7	14.7	14.7	22.1
	2.5	191.5	14.7	14.7	14.7	14.7	14.7	14.7	14.7	14.7	14.7	22.1
	3.0	220.9	22.1	14.7	14.7	14.7	14.7	14.7	22.1	14.7	14.7	22.1
With noise	0.5	22.1	14.7	22.1	14.7	22.1	22.1	22.1	22.1	22.1	7.4	22.1
	1.0	51.6	22.1	14.7	22.1	14.7	22.1	14.7	22.1	14.7	22.1	14.7
	1.5	125.2	22.1	14.7	22.1	14.7	22.1	14.7	22.1	14.7	14.7	22.1
	2.0	154.7	14.7	14.7	14.7	14.7	14.7	14.7	14.7	14.7	14.7	14.7
	2.5	221.0	14.7	22.1	29.5	14.7	14.7	14.7	22.1	22.1	14.7	22.1
	3.0	191.5	29.5	22.1	66.3	14.7	22.1	14.7	44.2	14.7	14.7	22.1

methods at all depths. Similarly, the improvements of the above three indices of LP are 3.3 dB, 1.0 times, and 0.4 dB, respectively.

From the results obtained by using the simulated data without and with noise in $\mathrm{SNR_{IS}}$ of -10 dB, it can be concluded that when using data processing methods in k-space to reconstruct PSFs within 3 mm, the results of NDFT and LP are generally better than those of the uniform resampling methods. In addition, the results of TDI ($\alpha=1$) and KBWC ($\alpha=2$) are suboptimal.

3.4. *Experimental verification*

The SS-OCT system used for the experiment can be found in our previous study[40] and the main parameters are listed in Table 4. Similar to the reference mirror, the sample is also a mirror. By changing the sample position, the $\boldsymbol{I}(\boldsymbol{k})$ at different depths (similar to the simulation) were collected and shown in Fig. 6.

Using Hilbert transformation, the phase difference $\Delta\boldsymbol{\Phi}$ can be calculated from the $\boldsymbol{I}(\boldsymbol{k})$ at depth z_0. According to the linear relationship between $\Delta\Phi$

Table 4. Parameters of SS-OCT experimental system.

Parameter	Value
Swept source	Axsun Co.
Sweeping rate	50 kHz
Center wavelength	1312 nm
Wavelength range	1259–1366
3 dB range	70 nm
Detector	PDB410C, Thorlabs Co.
Data acquisition card	PCI-5122, NI Co.

and k: $\Delta\boldsymbol{\Phi} = 2\boldsymbol{k}z_0$, the uniform $\boldsymbol{k}$ distribution can be obtained by uniform sampling of the $\Delta\Phi$. As shown in Fig. 7(a), the $\boldsymbol{k}$ distributions of the nonuniform sampling and the uniform resampling are shown in the black and red lines, respectively. Figure 7(b) shows the PSFs reconstructed from $\boldsymbol{I}(\boldsymbol{k})$s without processing (W/O pro) in $\boldsymbol{k}$-space. It can be seen that with the increment of imaging depth, the PSF gradually broadens, and the reconstruction quality degrades.

The PSFs reconstructed from $\boldsymbol{I}(\boldsymbol{k})$s processed with the six methods in k-space are shown in Fig. 8. It can be seen that all the methods can effectively suppress the broadening of PSF with the increment of imaging depth, which is conducive to keep the axial resolution. Relative to the results of W/O proc (Fig. 7(b)), LI, CSI, and KBWC ($\alpha = 2$) have while TDI has not increased the noise level.

The peak intensity, δ, and SNR of the PSFs at different depths are shown in Fig. 9. All the methods

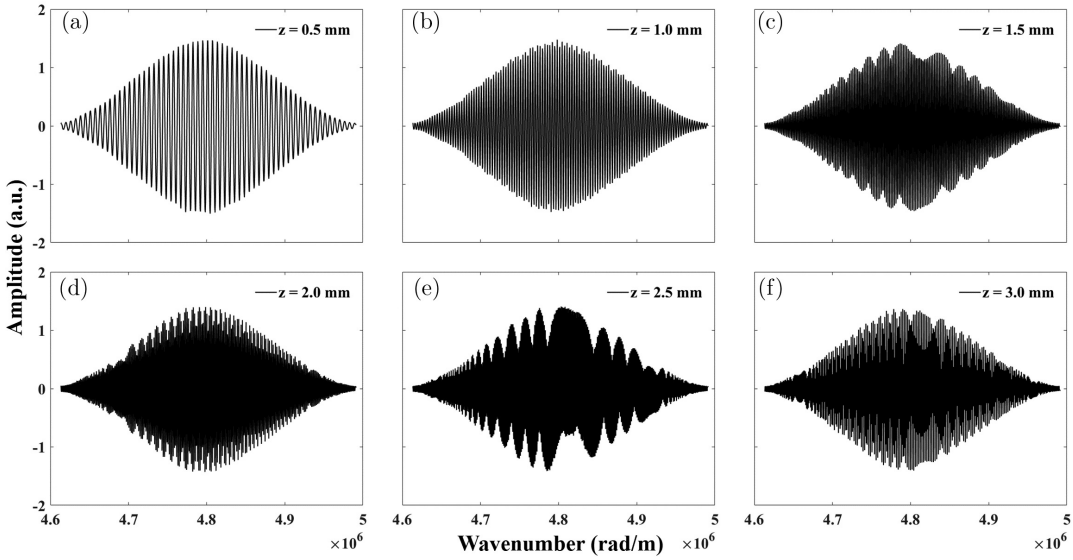

Fig. 6. Experimentally captured interference spectra at different depths.

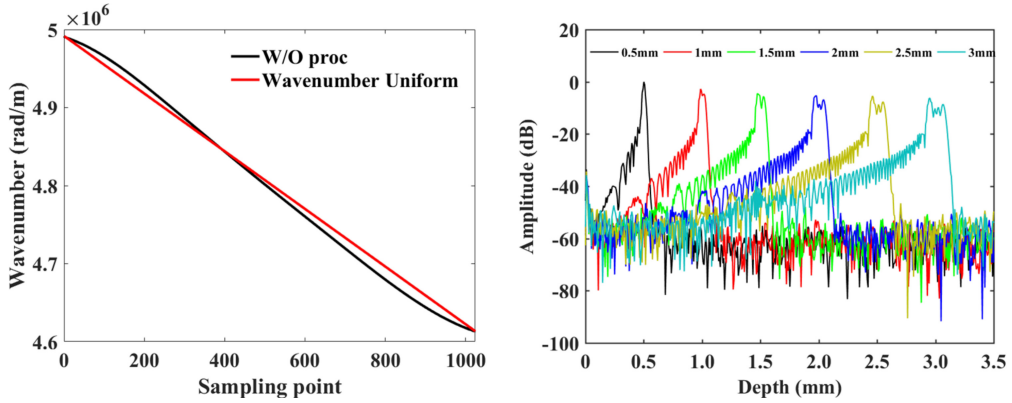

(a) (b)

Fig. 7. (a) k distributions under nonuniform sampling and uniform resampling and (b) reconstructed PSFs at different depths without processing.

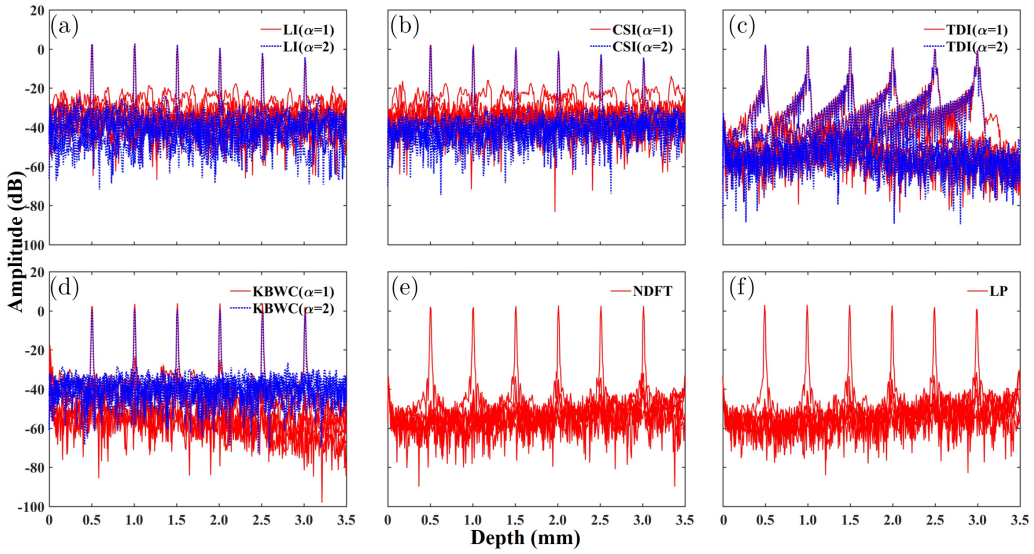

Fig. 8. PSFs at different depths reconstructed with different methods.

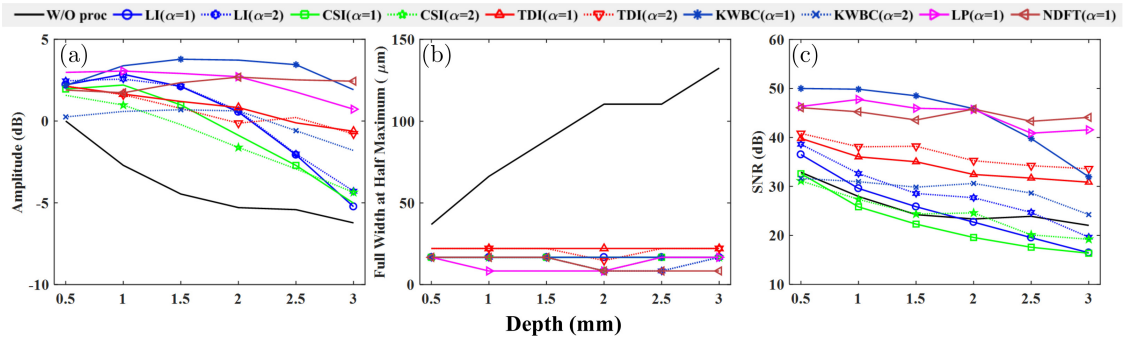

Fig. 9. (a) Peak intensity, (b) δ, and (c) SNR of PSFs at different depths reconstructed with different methods in k-space using experimental data.

can improve the peak intensity and δ, as shown in Figs. 9(a) and 9(b), respectively. Among these methods, TDI has the worst δ. In Fig. 9(a), the peak intensities of LP, NDFT, and KWBC ($\alpha = 1$) keep above 0 dB within 3 mm, and their fall-off within 3 mm are less than 6 dB. In Fig. 9(c), LP, NDFT, KWBC ($\alpha = 1$), and TDI ($\alpha = 2$) can effectively improve SNR. The detailed δ values of all the methods are shown in Table 5. For the results obtained with the experimental data, the improvements of the averaged peak intensity, δ and SNR of NDFT at depths from 0.5 to 3.0 mm are 1.9 dB, 1.4 times and 11.8 dB, respectively, compared to the averaged indices of all the uniform resampling

Table 5. Detailed δ values of different methods using experimental data (units: μm).

Depth (mm)	W/O proc	LI ($\alpha = 1$)	LI ($\alpha = 2$)	CSI ($\alpha = 1$)	CSI ($\alpha = 2$)	TDI ($\alpha = 1$)	TDI ($\alpha = 2$)	KWBC ($\alpha = 1$)	KWBC ($\alpha = 2$)	NDFT	LP
0.5	36.8	16.7	16.7	16.7	16.7	22.1	22.1	16.7	16.7	16.7	16.7
1.0	66.3	16.7	16.7	16.7	16.7	22.1	22.1	16.7	16.7	16.7	8.3
1.5	88.4	16.7	16.7	16.7	16.7	22.1	22.1	16.7	16.7	16.7	8.3
2.0	110.5	16.7	8.3	16.7	8.3	22.1	14.7	16.7	8.3	8.3	8.3
2.5	110.5	16.7	8.3	16.7	16.7	22.1	22.1	16.7	8.3	8.3	16.7
3.0	132.6	16.7	16.7	16.7	16.7	22.1	22.1	16.7	16.7	8.3	16.7

methods at all the depths. Similarly, the improvements of above three indices of LP are 2.0 dB, 1.4 times, and 11.7 dB, respectively.

The results obtained by using the simulated and experimental data show that the reconstruction quality of NDFT and LP is generally better than that of the uniform resampling methods in k-space under without or with noise. KWBC (a uniform resampling method) is prone to introduce interpolation errors, and KWBC ($\alpha = 1$) cannot effectively reconstruct the structure under $\mathrm{SNR_{IS}} = -10\,\mathrm{dB}$. In the experimental results, the SNR of KWBC ($\alpha = 1$) quickly decreases within the depth of 3 mm. However, the window effect in KWBC can reduce the sampling noise by averaging operation. So, the reconstruction quality of KWBC is instable and we should optimize the parameters of window size and α according to the degree of noise. LI and CSI are easy to introduce interpolation noise. TDI does not increase the noise level and has the worst δ in the experiment. Thus, the comparison of the axial PSFs at different depths demonstrates that NDFT and LP can be used as a benchmark for k-space data processing. In practical applications, especially under an even worse $\mathrm{SNR_{IS}}$ or at deeper imaging depth, the results will be helpful for the optimization and selection of data processing methods. In the future, we will focus on the quality of OCT images reconstructed by these methods.

4. Conclusion

In this study, the uniform resampling methods including LI, CSI, TDI, and KBWC, as well as the nonuniform sampling direct-reconstruction methods including LP and NDFT in k-space were used to reconstruct PSFs at different depths. The effect of the methods on the reconstruction quality was compared and analyzed by using simulated and experimental data. From the quantitative indices including the peak intensity, δ and SNR of PSFs at different depths, it was concluded that the reconstruction performance of NDFT and LP was generally better than that of the uniform resampling methods in k-space. Therefore, according to the imaging depth and the SNR_{IS} of interference spectrum, the obtained results will help us to optimize and select an appropriate data processing method in k-space, so as to improve the imaging quality of FD-OCT.

Acknowledgments

This project is supported by the National Natural Science Foundation of China (Grant Nos. 61575205 and 62175022), Sichuan Natural Science Foundation (2022NSFSC0803) and Sichuan Science and Technology Program (2021JDRC0035).

Conflicts of Interest

The authors declare that there are no conflicts of interest relevant to this article.

References

1. H. Hossein, C. C. Rosa, "Numerical study on spectral domain optical coherence tomography spectral calibration and re-sampling importance," *Photon. Sens.* **3**(1), 35–43 (2013).
2. S. Z. Yang, L. W. Liu, Y. X. Chang, N. N. Zhang, K. Liu, L. Hong, B. L. Chen, Y. Zhao, R. Hu, J. L. Qu, "*In vivo* mice brain microcirculation monitoring based on contrast-enhanced SD-OCT," *J. Innov. Opt. Health Sci.* **12**(1), 1950001 (2019).
3. F. J. Xing, J. H. Lee, C. Polucha, J. Lee, "Three-dimensional imaging of spatio-temporal dynamics of small blood capillary network in the cortex based on optical coherence tomography: A review," *J. Innov. Opt. Health Sci.* **13**(1), 2030002 (2020).
4. A. Abdurashitov, V. Tuchin, O. Semyachkina-Glushkovskaya, "Photodynamic therapy of brain tumors and novel optical coherence tomography strategies for *in vivo* monitoring of cerebral fluid dynamics," *J. Innov. Opt. Health Sci.* **13**(2), 2030004 (2020).
5. R. Leitgeb, F. Placzek, E. Rank, L. Krainz, R. Haindl, Q. Li, M. Liu, M. Andreana, A. Unterhuber, T. Schmoll, W. Drexler, "Enhanced medical diagnosis for doctors: A perspective of optical coherence tomography," *J. Biomed. Opt.* **26**(10), 100601 (2021).
6. E. Auksorius, D. Borycki, P. Stremplewski, K. Liewski, S. Tomczewski, P. Niedźwiedziuk, B. Sikorski, M. Wojtkowski, "*In vivo* imaging of human cornea with high-speed and high-resolution Fourier-domain full-field optical coherence tomography," *Biomed. Opt. Exp.* **11**(5), 2849–2865 (2020).
7. F. Faraldi, C. A. Lavia, M. Nassisi, R. A. Kilian, D. Bacherini, S. Rizzo, "Swept-source OCT reduces the risk of axial length measurement errors in eyes with cataract and epiretinal membranes," *PLOS ONE* **16**(9), e0257654 (2021).

8. K. Nagib, B. Mezgebo, N. Fernando, B. Kordi, S. S. Sherif, "Generalized image reconstruction in optical coherence tomography using redundant and non-uniformly-spaced samples," *Sensors* **21**(7057), 1–14 (2021).
9. N. Uribe-Patarroyo, S. H. Kassani, M. Villiger, B. E. Bouma, "Robust wavenumber and dispersion calibration for Fourier-domain optical coherence tomography," *Opt. Exp.* **26**(7), 9081–9094 (2018).
10. R. Leitgeb, C. K. Hitzenberger, A. F. Fercher, "Performance of Fourier domain vs. time domain optical coherence tomography," *Opt. Exp.* **11**(8), 889–894 (2003).
11. M. Wojtkowski, R. Leitgeb, A. Kowalczyk, T. Bajraszewski, A. F. Fercher, "*In vivo* human retinal imaging by Fourier domain optical coherence tomography," *J. Biomed. Opt.* **7**(3), 457–463 (2002).
12. C. Ding, P. Bu, X. Z. Wang, O. Sasaki, "A new spectral calibration method for Fourier domain optical coherence tomography," *Optik* **121**, 965–970 (2010).
13. K. Wang, Z. H. Ding, "Spectral calibration in spectral domain optical coherence tomography," *Chin. Opt. Letts.* **6**(12), 902–904 (2008).
14. X. L. Zhang, W. R. Gao, H. Y. Bian, C. L. Chen, J. L. Liao, "Self-spectral calibration for spectral domain optical coherence tomography," *Opt. Eng.* **52** (6), 063603-1-7 (2013).
15. M. A. Choma, K. Hsu, J. A. Izatt, "Swept source optical coherence tomography using an all-fiber 1300-nm ring laser source," *J. Biomed. Opt.* **10**(4), 044009-1-6 (2005).
16. C. M. Eigenwillig, B. R. Biedermann, G. Palte, R. Huber, "K-space linear Fourier domain mode locked laser and applications for optical coherence tomography," *Opt. Exp.* **16**(12), 8916–8937 (2008).
17. A. M. Davis, M. A. Choma, J. A. Izatt, "Heterodyne swept-source optical coherence tomography for complete complex conjugate ambiguity removal," *J. Biomed. Opt.* **10**(6), 064005 (2005).
18. J. Ren, H. K. Gille, J. Wu, C. H. Yang, "*Ex vivo* optical coherence tomography imaging of collector channels with a scanning endoscopic probe," *Invest. Opth. Vis. Sci.* **52**(7), 3921–3925 (2011).
19. J. F. Xi, L. Huo, J. S. Li, X. D. Li, "Generic real-time uniform K-space sampling method for high-speed swept-source optical coherence tomography," *Opt. Exp.* **18**(9), 9511–9517 (2011).
20. D. C. Adler, Y. Chen, R. Huber, J. Schmitt, J. Connolly, J. G. Fujimoto, "Three-dimensional endomicroscopy using optical coherence tomography," *Nat. Photon.* **1**(12), 709–716 (2007).
21. M. Mujat, B. H. Park, B. Cense, T. C. Chen, J. F. D. Boer, "Autocalibration of spectral-domain optical coherence tomography spectrometers for *in vivo* quantitative retinal nerve fiber layer birefringence determination," *J. Biomed. Opt.* **12**(4), 041205 (2007).
22. Z. Q. Xu, C. Lionel, M. Roman, "A zero-crossing detection method applied to Doppler OCT," *Opt. Exp.* **16**, 4394–4412 (2008).
23. T. Wu, Z. H. Ding, L. Wang, M. H. Chen, "Spectral phase based k-domain interpolation for uniform sampling in swept-source optical coherence tomography," *Opt. Exp.* **19**, 18430–18439 (2011).
24. M. Szkulmowski, M. Wojtkowski, T. Bajraszewski, I. Gorczynska, P. Targowski, W. Wasilewski, A. Kowalczyk, C. Radzewicz, "Quality improvement for high resolution *in vivo* images by spectral domain optical coherence tomography with supercontinuum source," *Opt. Commun.* **246**(4–6), 569–578 (2005).
25. Y. Chen, H. Zhao, Z. Wang, "Investigation on spectral-domain optical coherence tomography using a tungsten halogen lamp as light source," *Opt. Rev.* **16**(1), 26–29 (2009).
26. A. R. Tumlinson, B. Hofer, A. M. Winkler, B. Považay, W. Drexler, J. K. Barton, "Inherent homogenous media dispersion compensation in frequency domain optical coherence tomography by accurate k-sampling," *Appl. Opt.* **47**(5), 687–693 (2008).
27. D. Hillmann, G. Huttmann, P. Koch, Using nonequispaced fast Fourier transformation to process optical coherence tomography signals, *Proc. SPIE 7372 on Optical Coherence Tomography and Coherence Techniques IV*, (OPTICA Publishing Group, Munich, Germany, 2009), pp. 73720R1-6.
28. N. R. Lomb, "Least-squares frequency analysis of unequally spaced data," *Astrophys. Space Sci.* **39**(2), 447–462 (1976).
29. T. Wu, Z. H. Ding, K. Wang, C. Wang, "Swept source optical coherence tomography based on nonuniform discrete Fourier transform," *Chin. Opt. Lett.* **7**(10), 941–944 (2009).
30. T. Han, J. R. Qiu, D. Wang, J. Meng, Z. Y. Liu, Z. H. Ding, "Constrained polynomial fit-based k-domain interpolation in swept-source optical coherence tomography," *J. Innov. Opt. Health Sci.* **14**(1), 2140008 (2021).
31. A. Liu, R. Wang, K. L. Thornburg, S. Rugonyi, "Efficient postacquisition synchronization of 4-D nongated cardiac images obtained from optical coherence tomography: Application to 4-D reconstruction of the chick embryonic heart," *J. Biomed. Opt.* **14**(4), 044020–044011 (2009).
32. S. Vergnole, D. Lévesque, G. Lamouche, "Experimental validation of an optimized signal processing method to handle non-linearity in swept-source optical coherence tomography," *Opt. Exp.* **18**(10), 10447–10461 (2010).
33. B. E. Bouma, J. F. de Boer, D. Huang, I. K. Jang, T. Yonetsu, C. L. Leggett, R. Leitgeb, D. D. Sampson,

M. Suter, B. J. Vakoc, M. Villiger, M. Wojtkowski, "Optical coherence tomography," *Nat. Rev. Meth. Primers* **2**(1), 79 (2022).
34. W. H. Press, S. A. Teukolsky, W. T. Vetterling, B. P. Flannery, *Numerical Recipes in Fortran*, Cambridge University Publishing, New York (1992).
35. Y. D. Zhang, X. Q. Li, L. Wei, K. Wang, Z. H. Ding, G. H. Shi, "Time-domain interpolation for Fourier-domain optical coherence tomography," *Opt. Lett.* **34**(12), 1849–1851 (2009).
36. J. I. Jackson, C. H. Meyer, D. G. Nishimura, A. Macovski, "Selection of a convolution function for Fourier inversion using gridding computerised tomography application," *IEEE Trans. Med. Imaging* **10**(3), 473–478 (1991).
37. P. J. Beatty, D. G. Nishimura, J. M. Pauly, "Rapid gridding reconstruction with a minimal oversampling ratio," *IEEE Trans. Med. Imaging* **24**(6), 799–808 (2005).
38. K. Wang, Z. Ding, T. Wu, C. Wang, J. Meng, M. Chen, L. Xu, "Development of a non-uniform discrete Fourier transform based high speed spectral domain optical coherence tomography system," *Opt. Exp.* **17**(14), 12121–12131 (2009).
39. J. Y. Fan, F. Gao, W. Kong, H. W. Li, G. H. Shi, "A full spectrum resampling method in polygon tunable laser-based swept-source optical coherence tomography," *Acta. Phys. Sin.* **66**(11), 114204 (2017).
40. Y. Yang, X. Yue, Y. Zhang, "Optimal processing sequence and method combination of linear resampling and spectral shaping in swept-source optical coherence tomography," *Opt. Commun.* **484**, 126677 (2021).